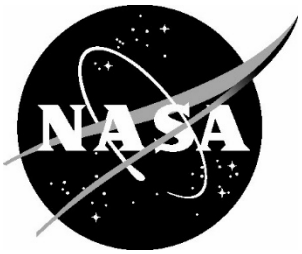
NASA/TM–20260001916



Quantifying the impacts of solar and geomagnetic activity on objects in LEO

Daniel, J. Gershman
NASA Goddard Space Flight Center, Greenbelt, MD

March 2026

NASA STI Program Report Series

Since its founding, NASA has been dedicated to the advancement of aeronautics and space science. The NASA scientific and technical information (STI) program plays a key part in helping NASA maintain this important role.

The NASA STI program operates under the auspices of the Agency Chief Information Officer. It collects, organizes, provides for archiving, and disseminates NASA's STI. The NASA STI program provides access to the NTRS Registered and its public interface, the NASA Technical Reports Server, thus providing one of the largest collections of aeronautical and space science STI in the world. Results are published in both non-NASA channels and by NASA in the NASA STI Report Series, which includes the following report types:

- TECHNICAL PUBLICATION. Reports of completed research or a major significant phase of research that present the results of NASA Programs and include extensive data or theoretical analysis. Includes compilations of significant scientific and technical data and information deemed to be of continuing reference value. NASA counterpart of peer-reviewed formal professional papers but has less stringent limitations on manuscript length and extent of graphic presentations.

- TECHNICAL MEMORANDUM. Scientific and technical findings that are preliminary or of specialized interest, e.g., quick release reports, working papers, and bibliographies that contain minimal annotation. Does not contain extensive analysis.

- CONTRACTOR REPORT. Scientific and technical findings by NASA-sponsored contractors and grantees.

- CONFERENCE PUBLICATION. Collected papers from scientific and technical conferences, symposia, seminars, or other meetings sponsored or co-sponsored by NASA.

- SPECIAL PUBLICATION. Scientific, technical, or historical information from NASA programs, projects, and missions, often concerned with subjects having substantial public interest.

- TECHNICAL TRANSLATION. English-language translations of foreign scientific and technical material pertinent to NASA's mission.

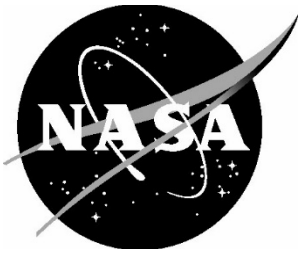
Specialized services also include organizing and publishing research results, distributing specialized research announcements and feeds, providing information desk and personal search support, and enabling data exchange services.

For more information about the NASA STI program, see the following:

- Access the NASA STI program home page at http://www.sti.nasa.gov

.

NASA/TM–20260001916



Quantifying the impacts of solar and geomagnetic activity on objects in LEO

Daniel, J. Gershman
NASA Goddard Space Flight Center, Greenbelt, MD

National Aeronautics and
Space Administration

NASA Goddard Space Flight Center
Greenbelt, MD

March 2026

The use of trademarks or names of manufacturers in this report is for accurate reporting and does not constitute an official endorsement, either expressed or implied, of such products or manufacturers by the National Aeronautics and Space Administration.

Available from:

NASA STI Program / Mail Stop 050
NASA Langley Research Center
Hampton, VA 23681-2199

Abstract. Increases in geomagnetic activity leads to rapid enhancements in atmospheric mass density and corresponding increases in orbital drag in Low Earth Orbit (LEO). Drag is highly orbit and object dependent, resulting in difficulties in developing a comprehensive yet operationalizable model. Here we combine publicly available orbital tracking data with proxies for energy inputs to the upper atmosphere to parameterize a simple relationship between these inputs and the corresponding drag acceleration for a given object in LEO. We then utilize predictions of energy inputs to calculate the expected orbital decay of that object for a specified level of geomagnetic activity. We apply this technique to the reentries of two objects of drastically different scale: the Tiangong-1 space station and Binar-1 CubeSat. Broad application of the presented approach could enable more robust object tracking, collision avoidance, and maneuver planning ahead of geomagnetic storms.

Introduction

Rapid changes in the upper atmosphere and their associated changes in drag acceleration and orbital decay severely complicate the tracking and control of satellites and objects in Low Earth Orbit (LEO) (see *Bruinsma et al.* [2023] and references therein). A major driver of these rapid changes is geomagnetic activity. The neutral density in LEO can increase by a factor of ~five during the most intense geomagnetic storms, with effects persisting for several days [*Zesta and Oliveira,* 2019]. Sudden increases in drag result in abrupt altitude losses that impact collision avoidance calculations and require last minute maneuvers [*Thayer et al.* 2021]. In addition, altitude loss during geomagnetic storms for active satellites must be compensated for by station-keeping maneuvers. Inefficient maneuvers with poor predictions of drag lead to increased fuel use [*Berger et al.* 2023]. Furthermore, geomagnetic storms accelerate object re-entry, and current propagation models cannot accurately take these dynamics into account [*Oliveira et al.* 2025]. Finally, rapid altitude loss can lead to tracking issues for uncontrolled objects, resulting in days of lost acquisitions and increased risk of unmonitored collisions [*Burke,* 2018].

The impact of increased atmospheric drag is not instantaneous but rather integrated over time to determine the net change in altitude of objects during geomagnetic storms [*Oliveira and Zesta,* 2019]. The decay in altitude is not only orbit and activity dependent, but also object dependent, which has complicated efforts for a generalized solution for quantifying the impacts of drag. The standard approach for orbit propagation combines independent estimates of the upper atmospheric state from a global thermosphere model with an object-specific ballistic coefficient to estimate drag acceleration [*Bruinsma et al.* 2023]. However, the propagation of uncertainties from model inputs to estimates of drag acceleration are highly non-linear and challenging to evaluate. Model performance can be improved with now-casts of the upper atmosphere incorporated via data assimilation techniques [*Storz et al.* 2005; *Bowman et al.* 2008], but this scaling further inhibits the ability to forecast how changes in drivers will lead to changes in drag.

Here we present an alternative approach, which is thermosphere-model agnostic and focuses on single object solutions rather than providing a global generalization. This methodology builds upon recent work by *Gershman* [2016] that demonstrated how variations in orbit-averaged thermospheric mass density and the corresponding object drag acceleration are well-represented by a linear combination of proxies of solar and geomagnetic energy input to the upper atmosphere. We will extend this parameterization to enable predictions of orbital decay for a

given object from predictions of energy input sources. We then model the uncontrolled re-entries of the Tiangong-1 space station module [*Pardini and Anselmo*, 2019] and Binar-1 CubeSat [*Downey et al.,* 2022; *Wang et al.,* 2025], demonstrating the applicability of this approach to modeling the drag acceleration and orbital decay of objects of drastically different scales. We then discuss potential applications using publicly available object tracking data and solar and geomagnetic energy source indices.

Modeling Drag Acceleration and Orbital Decay

We begin with the equation for the change of the semi-major axis (a) of an object in orbit in the presence of only drag [*Picone et al.,* 2005],

$$\frac{da}{dt} = \frac{2a^2 v}{\mu} \dot{\boldsymbol{v}}_{\boldsymbol{D}} \cdot \boldsymbol{e}_{\boldsymbol{v}} \qquad (1).$$

Here, v is the speed of the object, μ is the gravitational parameter ($3.986004418 \times 10^{14}$ m^3/s^2 for Earth), $\dot{\boldsymbol{v}}_{\boldsymbol{D}}$ is the drag acceleration, and $\boldsymbol{e}_{\boldsymbol{v}}$ is the object's unit velocity vector. The drag acceleration can be approximated as,

$$\dot{\boldsymbol{v}}_{\boldsymbol{D}} = -\frac{1}{2}\rho B |\boldsymbol{v} - \boldsymbol{V}|^2 \boldsymbol{e}_{\boldsymbol{v}-\boldsymbol{V}} \approx -\frac{1}{2}\rho B v^2 \boldsymbol{e}_{\boldsymbol{v}} \qquad (2),$$

where **V** is the velocity vector of the atmospheric motion, here simplified to be negligible compared to the orbital speed v. The inverse ballistic coefficient, B, is defined as,

$$B = \frac{C_D A}{m} \qquad (3).$$

where C_D is the drag coefficient, A is the effective area of the object, and m is the object mass.

The time-averaged (denoted as <>) drag acceleration can be determined for a given object using its tracking data such as Two-Line-Element (TLE) data following *Pincone et al.* [2005] (combining their equations (2), (8) and (12)) as,

$$\langle \dot{\boldsymbol{v}}_{\boldsymbol{D}} \rangle \approx -\frac{\frac{1}{3}\mu^{2/3}\langle n_M \rangle^{-1/3} \Delta n_M \langle v \rangle^2}{\int v^3 \left(1 - \frac{r\omega}{v}\cos i\right)^2 dt} \boldsymbol{e}_{\boldsymbol{v}} \qquad (4).$$

where n_m is the mean motion, ω is the rotation rate of Earth, i is the average orbit inclination, and Δn_m is the change in mean motion between reference time epochs, here taken as daily differences. The application of equation (4) is thermosphere-model-agnostic and does not require knowledge of object ballistic coefficient or atmospheric density, but rather only object tracking data. Equation (4) will be used to generate 'measured' drag acceleration values for a given object to be used in the parameter fits that will be discussed next.

As demonstrated by *Gershman* [2026], for objects with constant ballistic coefficients and altitude, the time-averaged drag acceleration can be simply parameterized in terms of solar and geomagnetic energy sources, S and G, respectively, as,

$$\langle \dot{\boldsymbol{v}}_{\boldsymbol{D}} \rangle \approx -(\alpha S + \beta G + \gamma)\boldsymbol{e}_{\boldsymbol{v}} \qquad (5).$$

For the case of relative variations in inverse ballistic coefficient or changes in altitude, we need to include additional factors in equation (5). Because drag acceleration is proportional to the inverse ballistic coefficient (B), we simply scale equation (5) by $B/\bar{B}$, where $\bar{B}$ is the average value over the parameterization interval, distinct from the <> time-average corresponding to orbit or daily averages). In addition, because mass density is typically modeled as varying exponentially with altitude, we include a corresponding factor in equation (5). We define a new fit parameter H that serves as this effective scale height. To accommodate objects with elliptical orbits, this altitude factor is defined in terms of the time-averaged semi-major axis (<a>) and a reference $\langle a \rangle_o$ that is taken as the time-averaged semi-major axis at the beginning of the time window used for the parameterization. Finally, we allow for a time shift in the geomagnetic energy input to account for a systematic delay in the energy driving a response in drag acceleration that is not captured by the pre-conditioning of G. Both scale height H and time shift T_o parameters must be positive. We do not apply a shift to the solar energy input since it varies more slowly and its heating effect is integrated over a longer period of time. This generalized averaged drag acceleration parameterization takes the form of,

$$\langle \dot{\boldsymbol{v}}_{\boldsymbol{D}} \rangle \approx -\left(\frac{B}{\bar{B}}\right) \exp\left(\frac{-(\langle a \rangle - \langle a \rangle_o)}{H}\right) (\alpha S(t) + \beta G(t - T_o) + \gamma)\boldsymbol{e}_{\boldsymbol{v}} \qquad (6).$$

Equation (6) therefore connects how global energy inputs drive drag acceleration for a given object. Because we use orbit-averaged or daily-averaged quantities, this equation applies to objects in LEO with elliptical orbits and $\langle a \rangle \approx R_E + \langle z \rangle$, where $\langle z \rangle$ is the average object altitude and R_E is the average radius of the Earth. From Kepler's Third Law, the semi-major axis $\langle a \rangle$ can be defined in terms of $\langle n_m \rangle$ as,

$$\langle a \rangle = \left(\frac{\mu}{\langle n_m \rangle^2}\right)^{1/3} \qquad (7).$$

We now return to equation (1) for objects with steady ballistic coefficients (i.e., $B/\bar{B} \sim 1$) and substituting in equation (6) for the drag acceleration we find,

$$\frac{d\langle a \rangle}{dt} \approx -\frac{2\langle a \rangle^2 \langle v \rangle}{\mu} \exp\left(\frac{-(\langle a \rangle - \langle a \rangle_o)}{H}\right) (\alpha S(t) + \beta G(t - T_o) + \gamma) \qquad (8).$$

Equation (8) can be numerically integrated to solve for the change in <a> over a given interval. However, it is also useful to obtain an analytical approximation for this quantity. We separate variables to each side and integrate to yield,

$$\int_{\langle a \rangle_1}^{\langle a \rangle_2} \frac{\exp\left(\frac{(\langle a \rangle - \langle a \rangle_o)}{H}\right)}{\langle a \rangle^2} \mathrm{d}\langle a \rangle \approx -\int_{t_1}^{t_2} \frac{2\langle v \rangle}{\mu} (\alpha S(t) + \beta G(t - T_o) + \gamma) dt \qquad (9),$$

where $\langle a \rangle_1$, and $\langle a \rangle_2$ are semi-major axes at times t_1, and t_2, respectively. We then perform the substitution ($u = \langle a \rangle - \langle a \rangle_o$) to find,

$$\int_{u_1}^{u_2} \frac{\exp\left(\frac{u}{H}\right)}{(u+\langle a\rangle_o)^2}\,du \approx -\int_{t_1}^{t_2} \frac{2\langle v\rangle}{\mu}(\alpha S(t) + \beta G(t-T_o) + \gamma)dt \quad (10).$$

Noting that $\langle a\rangle_o$ >> u and integrating, we find,

$$\frac{H}{\langle a\rangle_o{}^2}\left(\exp\left(\frac{(\langle a\rangle_2 - \langle a\rangle_o)}{H}\right) - \exp\left(\frac{(\langle a\rangle_1 - \langle a\rangle_o)}{H}\right)\right) \approx -\int_{t_1}^{t_2} \frac{2\langle v\rangle}{\mu}(\alpha S(t) + \beta G(t-T_o) + \gamma)dt \quad (11).$$

Finally, under the assumption that the object velocity $\langle v\rangle$ is nearly constant over the time integration (1 km of altitude drop in LEO corresponds to a change in velocity of less than 1 m/s) we rearrange equation (11) to solve for the change in semi-major axis ($\Delta\langle a\rangle = \langle a\rangle_2$-$\langle a\rangle_1$) as,

$$\Delta\langle a\rangle \approx \langle a\rangle_o - \langle a\rangle_1 + H\log\left(\exp\left(\frac{(\langle a\rangle_1 - \langle a\rangle_o)}{H}\right) - \frac{2v\langle a\rangle_o{}^2}{\mu H}\left((t_2-t_1)\gamma + \alpha\Phi_S + \beta\Phi_G\right)\right) \quad (12),$$

where $\Phi_S \equiv \int_{t_1}^{t_2} S(t)dt$ and $\Phi_G \equiv \int_{t_1}^{t_2} G(t-T_o)dt$.

Equations (8) and (12) describe the change in semi-major axis for an object given a set of time-integrated energy sources *S* and *G* and drag acceleration parameters: α, β, γ, *H,* and T_o. No thermosphere model or absolute quantification of the object's ballistic coefficient is used in these calculations as ρ and *B* are embedded within the parameters that are fit from the data.

Variations in Energy Sources

Since object tracking data is updated several times daily and the impact of geomagnetic storms can last multiple days, we consider time interval of (t_2-t_1) of 48 hours. Here, following *Gershman* [2026], we use TIMED/SEE E10.7 [*Woods et al.,* 2005] and AMPERE total field-aligned current (FAC) data [*Anderson et al.,* 200] for *S* and *G*, respectively. We pre-condition these datasets by low-pass-filtering the E10.7 data with a time constant of 18 hours, and by subtracting a background 0.5MA offset from the AMPERE data and then low-pass-filtering with a time constant of 48 hours. To put values of Φ_G in the context of geomagnetic activity, Figure 1 shows a histogram of integrated geomagnetic energy from representative AMPERE data as a function of the minimum Dst index observed within the corresponding 48 hour period. For extreme events such as the Gannon Storm in May 2014 with a Dst reaching -412 nT [*Hayakawa et al.,* 2025], Φ_G reaches ~2x10^6 MA·s. Typical intense storm, moderate storm, and quiet-time values are ~8x10^5 MA·s, ~5x10^5 MA·s, and ~10^5 MA·s respectively. These ranges can be used in equations (8) and (12) to inform the potential for orbital decay for a given level of geomagnetic activity even if accurate predictions of *G* are not available.

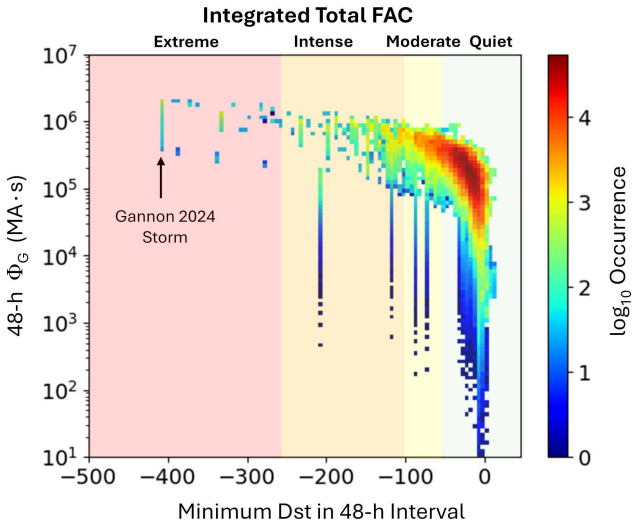


Figure 1. Histogram of Φ_G derived from selected representative subsets of AMPERE total FAC data for different levels of activity between 2009 through 2024 as a function of the minimum Dst observed during the relevant 48 hour interval Φ_G reaches ~2x10^6 MA·s during extreme geomagnetic storms, with typical values in the ~10^5 to 10^6 MA·s range.

Demonstration

We apply the drag parameterization and analytical model of orbital decay from the above section to two LEO objects. The first is the Tiangong-1 space station module (mass of 8506 kg) that re-entered Earth's atmosphere uncontrollably in April 2018. The second is the Binar 1 CubeSat (mass of 1.33 kg) that was deployed from the International Space Station (ISS) in October 2021 and re-entered in September 2022. We first use daily-averaged TLE data for each object and apply equation (4) to calculate the drag acceleration. We then parameterize variations in $\langle \dot{\boldsymbol{v}}_{\boldsymbol{D}} \rangle$ using S and G energy inputs terms to solve for α, β, γ, H, and T_o at each point using the previous 27 days of measured data, accounting for a solar rotation. As discussed by *Gershman* [2026], this parameterization time interval can be adjusted, though 27 days was found to provide a reasonable balance between seasonal variations and capturing sufficient structure to avoid overfitting. We assume $B/\bar{B}\sim 1$. As shown in Figure 2, the drag acceleration of both objects is successfully parameterized using this approach. We found that $T_o \sim 1$ day for the Tiangong-1 case at solar minimum and $T_o \sim 0$ days for the Binar-1 case at solar maximum.

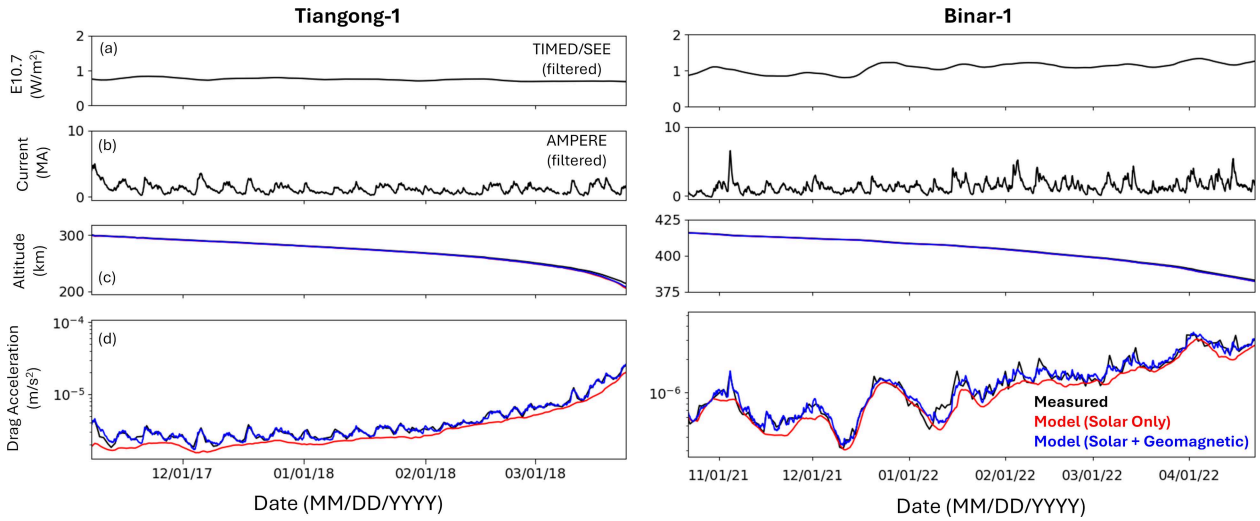


Figure 2. (a) solar energy proxy S, (b) geomagnetic energy proxy G, (c) daily-averaged altitude $\langle z \rangle$, and (d) daily-averaged drag acceleration $\langle \dot{\boldsymbol{v}}_{\boldsymbol{D}} \rangle$ for the Tiangong-1 space station module (left panels) and the Binar-1 CubeSat (right panels). The measured drag acceleration is shown in black. The parameterized drag acceleration including only α, γ, H, and T_o is shown in red and corresponds to the geomagnetically quiet case, tracking the lower envelope of the measured acceleration. The blue curve includes all parameters and accurately captures the small-scale variations in drag acceleration associated with geomagnetic energy input into the upper atmosphere.

With known α, β, γ, H, and T_o parameters, for each data point we now apply equation (8) to calculate the change in semi-major axis expected in the next 48 hours. Because these are historical events, we use the measured S and G for 48 hours in the future in this calculation to validate this approach. These results are shown in Figure 3 for the two objects. In addition to using the measured G, we take typical values of G in equation (12) to develop contours of potential orbital decay under different geomagnetic conditions. The 'extreme' case appropriately represents a limit of the largest possibly orbital decay. The curve associated with 'intense' geomagnetic activity bounds the Tiangong-1 variations due to its re-entry during solar minimum. The 'intense' curve is more closely approached during a large geomagnetic storm present in the Binar-1 data. These examples demonstrate that even when precise predictions of G are not available, the orbital decay expected for an object can be reasonably constrained. Close to re-entry for the Tiangong-1 module, even small variations in G associated with geomagnetic substorms can lead to rapid, kilometer-scale changes in satellite altitude.

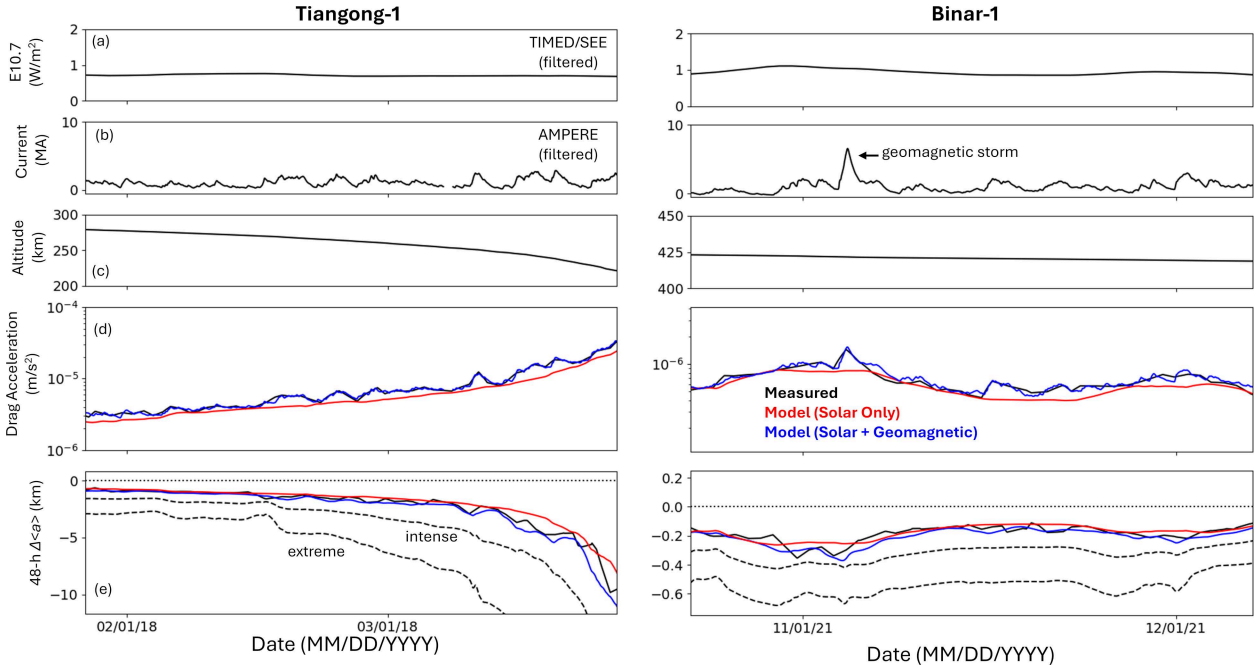


Figure 3. (a) solar energy proxy S, (b) geomagnetic energy proxy G, (c) daily-averaged altitude <z>, (d) daily-averaged drag acceleration $\langle \dot{\boldsymbol{v}}_{\boldsymbol{D}} \rangle$ and (e) change in semi-major axes over the subsequent 48 hours for the Tiangong-1 space station module (left panels) and the Binar-1 CubeSat (right panels). In panel (e) the black curve corresponds to the measured change from TLE tracking data. The red curve corresponds to the $G = 0$ (i.e., geomagnetically quiet) case that provides an upper envelope of the orbital decay, and the blue curve corresponds to the measured G case. The close match between the black and blue curves demonstrate the effectiveness of equation (12) in modeling orbital decay associated with geomagnetic activity. Dashed lines in panel (e) correspond to typical values of G associated with different levels of geomagnetic activity, with intense activity using $G \sim 8\text{x}10^5$ MA·s and extreme activity using $G \sim 2\text{x}10^6$ MA·s.

Discussion

As discussed by *Gershman* [2026], because $\langle \dot{\boldsymbol{v}}_{\boldsymbol{D}} \rangle$ is taken as a simple linear combination of input energy sources, the propagation of uncertainties in S and G to estimates of drag acceleration are straightforward. However, there can be significant systematic errors, data gaps, and maneuvers and/or attitude changes present in the reference tracking dataset that leads to systematic errors in the parameterization coefficient. Taking the public TLE data as an example, it was found that daily averaging was needed to obtain reliable results despite tracking data being updated several times daily for some objects. The goodness-of-fit in the parameterization process (e.g., the root-mean-square-percent-error or RMSPE) can be used to inform data quality and success of the parameterization. A high RMSPE indicates issues with either the tracking data quality or the underlying assumptions that go into the parameterization. As an example, the assumption of $B/\bar{B} \sim 1$ is not necessarily valid for the Starlink satellites, which can undergo significant changes in drag configurations associated with a change in effective area [*Berger et al.,* 2023; *Fitzpatrick et al.,* 2025] that would need to be accounted for before a successful parameterization could be achieved. If $B/\bar{B}$ were known for a given object then its variations could be incorporated into equation (6) before performing the parameterization fit. High RMSPE values are also expected for objects that are constantly maneuvering (i.e., at least once per day). Conversely, a low

RMSPE indicates a higher quality fit and successful parameterization process. In this sense, the goodness-of-fit provides an indication of which objects have semi-stable ballistic coefficients over a given period, and therefore provides a method of filtering a set of objects that could be useful for thermospheric inversion. A cursory analysis using public TLE data from ~30,000 tracked objects and a parameterization 27-day interval from April 18 through May 15, 2024 shows that the drag accelerations of thousands of objects are well represented (i.e., RMSPE <20%) by a linear combination of energy sources.

Variations of the time shift parameter (T_o) with object type, solar activity, and orbit plane likely warrant further study. The ~1 day shift required to fit the Tiangong-1 data may be indicative of how energy redistributes around the thermosphere differently during quiet times than active ones. For example, *Zesta and Oliveira* [2019] showed that heating times are significantly slower for weaker storms compared to other geomagnetically active time periods. In addition, *Weimer et al.* [2011] presented a simple model of the global thermospheric temperature that includes different time constants for heating and cooling rates, as well as an amplitude-dependent corrections. More advanced pre-processing of *G* that takes into account these processes may ultimately eliminate the need to include a time shift parameter.

Accurate predictions of energy inputs are critical for accurate predictions of drag acceleration and corresponding orbital decay. Because *S* varies more slowly and with clear periodicity associated with solar rotations, short-term predictions on the scale of ~48 hours are more readily accomplished. Appropriate real-time data streams for *G* are currently highly limited. Furthermore, predictions of such a dynamic quantity are challenging to achieve. Here the use of ranges of Φ_G associated with different levels of geomagnetic activity can provide solid constraints on the likely ranges of orbital decay even in the absence of reliable current and predicted geomagnetic energy input data sources.

Finally, while equation (8) provides an analytical estimate of orbital decay in the presence of only drag, the predicted $\langle \dot{\boldsymbol{v}}_{\boldsymbol{D}} \rangle$ over several days could also be used in conjunction with an additional term to model the effectiveness of satellite maneuvers. In such a case, numerical integration techniques could be used to propagate the satellite orbit and examine the timing and duration of an altitude-adjustment maneuver needed to compensate for the expected drag, or to avoid a potential collision. Here, the ranges of potential geomagnetic energy input can be used to constrain the optimal properties of the maneuver, with further improvements expected to become possible as real-time data streams and improved predictions of *G* become available.

Concluding Remarks

We have presented a technique to accurately quantify orbital decay for objects in LEO. We first parameterize drag acceleration for a given object using recent tracking data and proxies for energy sources associated with solar and geomagnetic activity. We then use predictions of energy sources to predict future changes in object altitude. This approach is immediately applicable for modeling orbital decay of thousands of currently tracked objects, in particular debris and satellites that are not actively maneuvering or rapidly altering their ballistic

coefficients. Improved prediction of drag and quantification of altitude loss can lead to more effective collision avoidance modeling and object tracking, enabling a safer LEO environment.

Acknowledgements. This work was supported by NASA Heliophysics. We gratefully acknowledge A. Glocer, D. Oliveira, and E. Zesta for their review and valuable feedback on this work. TLEs were downloaded from http://space-track.org/

References

Anderson, B. J., Takahashi, K., & Toth, B. A. (2000). Sensing global Birkeland currents with iridium® engineering magnetometer data. *Geophysical Research Letters,* 27(24), 4045–4048. https://doi.org/10.1029/2000gl000094

Berger, T. E., Dominique, M., Lucas, G., Pilinski, M., Ray, V., Sewell, R., et al. (2023). The thermosphere is a drag: The 2022 Starlink incident and the threat of geomagnetic storms to low earth orbit space operations. *Space Weather*, 21, e2022SW003330. https://doi.org/10.1029/2022SW003330

Bowman, B., Tobiska, W. K., Marcos, F., Huang, C., Lin, C., & Burke, W. (2008). A new empirical thermospheric density model JB2008 using new solar and geomagnetic indices. In *AIAA/AAS Astrodynamics Specialist Conference and Exhibit*, Honolulu, Hawaii. https://doi.org/10.2514/6.2008-6438

Bruinsma, S., Dudok de Wit, T., Fuller-Rowell, T., Garcia-Sage, K., Mehta, P., Schiemenz, F., et al. (2023). Thermosphere and satellite drag. *Advances in Space Research*. https://doi.org/10.1016/j.asr.2023.05.011

Burke, W. J. (2018). Thermospheric dynamics during the March 1989 magnetic storm. Balkan, Black sea and Caspian sea regional network for space weather studies. https://doi.org/10.31401/SunGeo.2018.02

Downey, F., Buchan, S., Hartig, B., Busan, D., Cook, J., Howie, R., et al. (2022). Binar Space Program: Binar-1 results and lessons learned. *Small Satellite Conference*. Retrieved from https://digitalcommons.usu.edu/smallsat/2022/all2022/56

Fitzpatrick, D. J., Sutton, E.K., Pilinski, M. D., et al. (2025), Harnessing Satellite Constellations as Signals of Opportunity for an Enhanced Specification of the Satellite Drag Environment in the Critical LEO Regime. *Authorea.* https://doi.org/10.22541/au.176244733.31846582/v1

Gershman, D. J. (2026), Parameterization of Satellite Drag Acceleration Without the Use of A Global Thermosphere Model, *NASA Technical Memorandum*, NASA/TM-20250011658, https://dx.doi.org/10.64631/LUGN8147

Hayakawa, H., Ebihara, Y., Mishev, A., Koldobskiy, S., Kusano, K., Bechet, S., Yashiro, S., Iwai, K., Shinbori, A., Mursula, K., Miyake, F., Shiota, D., Silveira, M. V. D., Stuart,

R., Oliveira, D. M., Akiyama, S., Ohnishi, K., Ledvina, V., & Miyoshi, Y. (2025). The Solar and Geomagnetic Storms in May 2024: A Flash Data Report. The Astrophysical Journal, 979 (1). https://doi.org/10.3847/1538-4357/ad9335

Oliveira, D. M., & Zesta, E. (2019). Satellite orbital drag during magnetic storms. *Space Weather*, 17, 1510–1533. https://doi.org/10.1029/2019SW002287

Oliveira, D. M., Zesta, E., & Garcia-Sage, K. (2025). Tracking Reentries of Starlink Satellites During the Rising Phase of Solar Cycle 25. Frontiers in Astronomy and Space Sciences, 12. https://doi.org/10.3389/fspas.2025.1572313

Pardini C. and Anselmo L., (2019), Monitoring the orbital decay of the Chinese space station Tiangong-1 from the loss of control until the re-entry into the earth's atmosphere, *Journal of Space Safety Engineering*. 6, 4, 265–275, https://doi.org/10.1016/j.jsse.2019.10.004.
Picone, J. M., J. T. Emmert, and J. L. Lean (2005), Thermospheric densities derived from spacecraft orbits: Accurate processing of two-line element sets, *J. Geophys. Res.*, 110, A03301, doi:10.1029/2004JA010585.

Storz, M. F., Bowman, B. R., Branson, M. J. I., Casali, S. J., & Tobiska, W. K. (2005). High accuracy satellite drag model (HASDM). *Advances in Space Research*, **36**(12), 2497–2505. https://doi.org/10.1016/j.asr.2004.02.020

Thayer, J.P., Tobiska, W.K., Pilinski, M.D. and Sutton, E.K. (2021). Remaining Issues in Upper Atmosphere Satellite Drag. In Space Weather Effects and Applications (eds A.J. Coster, P.J. Erickson, L.J. Lanzerotti, Y. Zhang and L.J.
Paxton). https://doi.org/10.1002/9781119815570.ch5

Wang, X., Wang, R., Wang, K., Yang, Z., Ren, T., Cao, J., et al. (2025). Premature reentry of the Binar CubeSats due to underestimation of solar and geomagnetic activities and its implication for importance of medium- and long-term space weather forecasts. *Space Weather*, 23, e2025SW004619. https://doi.org/10.1029/2025SW004619

Weimer, D. R., B. R.Bowman, E. K.Sutton, and W. K.Tobiska (2011), Predicting global average thermospheric temperature changes resulting from auroral heating, J. Geophys. Res., 116, A01312, doi:10.1029/2010JA015685.

Woods, T. N., F. G. Eparvier, S. M. Bailey, P. C. Chamberlin, J. Lean, G. J. Rottman, S. C. Solomon, W. K. Tobiska, and D. L. Woodraska (2005), Solar EUV Experiment (SEE): Mission overview and first results, *J. Geophys. Res.*, 110, A01312, doi:10.1029/2004JA010765.

Zesta, E., & Oliveira, D. M. (2019). Thermospheric heating and cooling times during geomagnetic storms, including extreme events. *Geophysical Research Letters*, 46, 12739–12746. https://doi.org/10.1029/2019GL085120